ARTICLE OPEN

Check for updates

Hyperactivity of subicular parvalbumin interneurons drives early amyloid pathology and cognitive deficits in Alzheimer's disease

Yan-Bing Chen[1,2,5], Bo Jiang[3,5], Kai Zhuang[1,5], He Wang[3,4,5], Hui-Min Peng[1], Bo-Wen Zhong[3,4], Wen-Ting Xie[1], Kai-Wei Chen[1], Ting-Ting Zou[1], Ya Wang[1], Hui-Li Yang[1], Qingwei Yang[1], Jiechao Zhou[1], Li Zhong[1]✉, Li-Hua Zhang[3]✉ and Jie Zhang[1,2]✉

Atrophy of the subiculum is the earliest hippocampal anatomical marker of Alzheimer's disease (AD) and is closely associated with early cognitive decline. However, the underlying mechanisms driving this vulnerability remain unclear. In this study, using the 5×FAD mouse model, we identified significant amyloid-beta (Aβ) accumulation in the subiculum during the early stages of AD. Through a combination of laser microdissection and proteomic analysis, we uncovered early dysregulation of GABAergic neurons in the subiculum. Further investigation revealed that parvalbumin (PV) interneurons (PV-INs) were key drivers of Aβ pathology, exhibiting pronounced hyperactivity during the initial stages of AD. Targeted inhibition of this PV interneuron hyperactivity at the onset of AD, using chemogenetic approaches and PV downregulation, significantly reduced Aβ accumulation in the subiculum and connected brain regions, while also enhancing cognitive function in AD mice. Supporting these findings, single-nucleus RNA sequencing (snRNA-seq) data from human AD patients revealed that PV expression in GABAergic neurons peaks at early stages of the disease, further reinforcing the role of PV interneuron hyperactivity in early AD progression. Additionally, PV interneuron inhibition restored protein homeostasis by normalizing GABAergic synapses, improving lysosomal function, and promoting APP degradation via K63-linked ubiquitination. These results provide critical insights into the cellular mechanisms that drive early Aβ pathology in the subiculum, positioning subicular PV-INs as promising therapeutic targets for early intervention in AD.

Molecular Psychiatry; https://doi.org/10.1038/s41380-025-03217-4

INTRODUCTION

Alzheimer's disease (AD) is the most prevalent neurodegenerative disorder characterized by progressive cognitive decline. Its key pathological features include the accumulation of amyloid-β (Aβ) plaques, formation of neurofibrillary tangles, and consequent neuronal loss [1]. In the later stages of AD, widespread neuronal loss becomes irreversible, highlighting the importance of early intervention to prevent or delay disease progression [2]. Aβ, an early pathological hallmark of AD, is generated via sequential cleavage of amyloid precursor protein (APP) by β-site secretase enzyme 1 (BACE1) and γ-secretase [3, 4]. As a result, the accumulation of Aβ in specific brain regions is thought to trigger downstream neurodegenerative processes, ultimately leading to the widespread neuronal damage observed in AD patients [5].

Among these affected regions, the subiculum—an integral part of the hippocampus—has been identified as one of the earliest sites of Aβ accumulation, particularly during the initial stages of the disease [6, 7]. The subiculum plays a critical role in memory retrieval and spatial navigation [8, 9], making its dysfunction highly relevant to the cognitive decline observed in AD. Atrophy of the subiculum is the earliest hippocampal anatomical marker of AD [10], with early Aβ deposition in this region closely linked to early neuronal loss, dendritic atrophy, and network hypersynchrony [11–13]. A growing body of evidence has also demonstrated that Aβ accumulation in the subiculum leads to neural hyperexcitability [14], a phenomenon observed in both AD patients and animal models, where it is closely associated with cognitive deficits [15–17]. In AD mouse models such as TgAPPArc and APP/PS1, Aβ pathology appears in the subiculum before other regions, coinciding with the onset of cognitive impairments [12, 15]. Despite these observations, the cellular mechanisms driving Aβ pathology in the subiculum remain unclear. In particular, whether specific neuronal subtypes contribute to the initiation or spread of Aβ pathology remains unknown. Furthermore, lesion studies in AD mouse models suggest that the subiculum may not only be an early site of Aβ accumulation but also a critical hub for propagating pathology to other connected brain regions, such as the CA1 region of the hippocampus and the retrosplenial cortex [15]. Understanding the mechanisms that drive early Aβ accumulation in the subiculum is thus essential, as it

[1]Department of Neurology, Zhongshan Hospital of Xiamen University, and Fujian Provincial Key Laboratory of Neurodegenerative Disease and Aging Research, Institute of Neuroscience, School of Medicine, Xiamen University, Xiamen, Fujian 361102, China. [2]Institute of Neuroscience, Fujian Medical University, Fuzhou, Fujian, China. [3]State Key Laboratory of Medical Proteomics, National Chromatographic R. & A. Center, CAS Key Laboratory of Separation Science for Analytical Chemistry, Dalian Institute of Chemical Physics, Chinese Academy of Sciences, Dalian 116023, China. [4]University of Chinese Academy of Sciences, Beijing 100049, China. [5]These authors contributed equally: Yan-Bing Chen, Bo Jiang, Kai Zhuang, He Wang. ✉email: zhongli@xmu.edu.cn; lihuazhang@dicp.ac.cn; jiezhang@xmu.edu.cn

Received: 15 April 2025 Revised: 29 July 2025 Accepted: 28 August 2025
Published online: 06 September 2025

could reveal novel targets for therapeutic interventions aimed at preventing or delaying AD progression during its earliest stages.

To explore the mechanisms driving Aβ pathology in the subiculum, we applied laser microdissection and data-independent acquisition (DIA) proteomics in 5×FAD mice. We found significant dysfunction in GABAergic neurons and lysosomal pathways from early to late AD stages. During early AD, PV-INs emerged as key regulators of Aβ accumulation. By employing chemogenetic inhibition and shRNA-mediated knockdown of PV expression, we effectively reduced PV interneuron activity, leading to a decrease in Aβ pathology and an improvement in cognitive function in AD mice. Analysis of snRNA-seq data from human AD brains revealed increased PV expression during early stages, further supporting the critical role of PV-INs in early Aβ pathology. Proteomic analysis also showed that inhibiting PV hyperactivity restored GABAergic and lysosomal function, along with a marked reduction in APP levels, which likely contributed to the observed decrease in Aβ pathology. Further analysis of this change in APP primarily indicates that the lysosome-dependent ubiquitination degradation pathway has been enhanced.

In conclusion, this study reveals the critical role of PV-INs in driving early Aβ pathology in the subiculum and suggests that targeting PV-INs activity can reduce Aβ accumulation and improve cognitive function. These findings provide valuable insights into early subicular pathology and highlight a potential therapeutic approach for preventing or delaying AD progression.

RESULTS

Early Aβ accumulation in the subiculum is linked to disruptions in GABAergic neurons and lysosomal function in 5×FAD mice

The subiculum is the earliest hippocampal region to undergo neuronal loss and atrophy in AD patients, with significant early Aβ deposition [6, 10, 11]. To explore whether Aβ deposition affects different brain regions at distinct stages of the disease, we systematically evaluated Aβ accumulation across multiple brain areas in the 5×FAD mouse model of AD. Notably, our analysis revealed significantly higher levels of Aβ deposition in the subiculum of 3-month-old 5×FAD mice compared to other brain regions (Fig. S1A, B). Focusing on the hippocampus, we examined Aβ deposition across its subregions—CA1, CA2, CA3, DG, and the subiculum—at 3, 6, and 12 months of age. The subiculum emerged as the earliest site of significant Aβ accumulation, with deposition detected as early as 3 months. In contrast, other hippocampal regions exhibited Aβ pathology at later stages (Fig. 1A, B). As the disease advanced, Aβ deposition increased in all regions, but the subiculum consistently showed the highest levels (Fig. 1A, B), indicating its unique vulnerability.

To explore the molecular mechanisms driving selective Aβ deposition in the subiculum during the early stages of AD, we performed data-independent acquisition–based mass spectrometry (DIA-MS) with deeper quantitative coverage to comprehensively profile proteomic changes and analyzed subiculum tissue microdissected from wild-type (WT) and 5×FAD (AD) mice at 3, 6, and 12 months (Fig. 1C and data file S1). This method provided enhanced reproducibility and coverage compared to the label-free quantitative method, with reduced missing data, facilitating the identification of low-abundance proteins [18]. Using this method, we identified 8948 protein groups across the subiculum samples, with each sample containing over 4000 quantified proteins. The technical reproducibility was high, with the coefficient of variation (CV) among biological replicates below 10%, and strong correlations were observed between replicates (Fig. S1C–E), indicating reproducible and reliable experimental conditions. A total of 992 differentially expressed proteins (DEPs) ($p < 0.05$) were identified across 3, 6, and 12 months by ANOVA, with DEPs ranging from high to intermediate abundance, reflecting the difficulty in reaching statistical significance for low-abundance proteins (Fig. S1F and data file S1). Principal component analysis (PCA) showed that samples clustered according to age, with PC1 accounting for 35.2% of the variance and effectively distinguishing between 3, 6, and 12 months (Fig. 1D). Analysis of the Aβ tryptic peptide (LVFFAEDVGSNK) confirmed significant Aβ increases in the subiculum of AD mice at 3, 6, and 12 months (Fig. 1E). A total of 161, 410, and 443 DEPs (fold change >1.2 or <0.83 and $p < 0.05$) (data file S1) were identified at 3 months, 6 months, and 12 months, respectively. Among these, 39 DEPs were consistently altered across all three age groups (Figs. 1F, S1G–J and data file S1). Gene ontology (GO) enrichment analysis revealed that these proteins were associated with key AD-related processes, including Aβ binding, lysosomal function, and regulation of neuronal death (Fig. 1G). Notably, comparison with other hippocampal proteomes [19] revealed that the subiculum exhibited significant proteomic changes as early as 3 months in AD mice, while hippocampal samples from both WT and AD mice at 5 months did not show similar alterations (Fig. S1K). This indicates that the subiculum is particularly vulnerable to early AD pathology, even ahead of the broader hippocampal regions.

To gain a comprehensive understanding of the subicular proteome, we conducted a weighted gene co-expression network analysis (WGCNA) to identify protein groups associated with AD pathogenesis. This analysis classified the quantified proteins into 22 co-expression modules, based on their correlation with the AD versus WT conditions (Fig. 2A). Of these, three modules exhibited significant differential expression between AD and WT mice. Notably, the pink and yellow modules were strongly upregulated, featuring proteins such as Gaa, Acp2, Apoe, and Hexb, which are primarily involved in lysosomal pathways, protein transport, and metabolic processes (Fig. 2B–E and data file S2). In contrast, the darkred module was downregulated and contained proteins such as Stxbp1, Slc6a1, and Cltc, which are related to GABAergic synaptic function and synaptic transmission (Fig. 2B–E and data file S2).

To further dissect the molecular pathways contributing to AD progression, we performed hierarchical clustering on proteins meeting a significance threshold of $p < 0.05$. This revealed eight distinct clusters, each grouping proteins with unique abundance patterns and functional roles (Fig. S2A, B). Clusters 2 and 3 showed upregulation, while clusters 6 and 8 exhibited downregulation during AD progression. Strikingly, clusters 3 and 6 were closely associated with lysosomal pathways and GABAergic synaptic dysfunction (Fig. S2A, B), aligning with the WGCNA findings.

In summary, these findings reinforce the subiculum as one of the earliest brain regions to exhibit vulnerability to Aβ accumulation in AD. The observed pathology, coupled with profound disruptions in lysosomal function and GABAergic synaptic activity, underscores a potential link between inhibitory neurons in the subiculum and the initial pathological mechanisms of AD.

Subicular PV-INs exhibit early hyperactivity and regulate Aβ pathology in AD mice

Our proteomic profiling of the subiculum highlighted early disruptions in GABAergic neurons, raising two possible hypotheses: either inhibitory neurons actively regulate early Aβ pathology, or they are particularly vulnerable to pathological changes driven by Aβ accumulation. To test these possibilities, we first mapped the distribution of major inhibitory neuron populations in the subiculum. Using Gad2-Cre;Ai14 mice, we analyzed three key inhibitory interneuron subtypes—parvalbumin-expressing (PV-INs), somatostatin-expressing (SST-INs), and vasoactive intestinal polypeptide-expressing (VIP-INs). Among these, PV-INs were the most abundant, comprising 47.1% of the total inhibitory

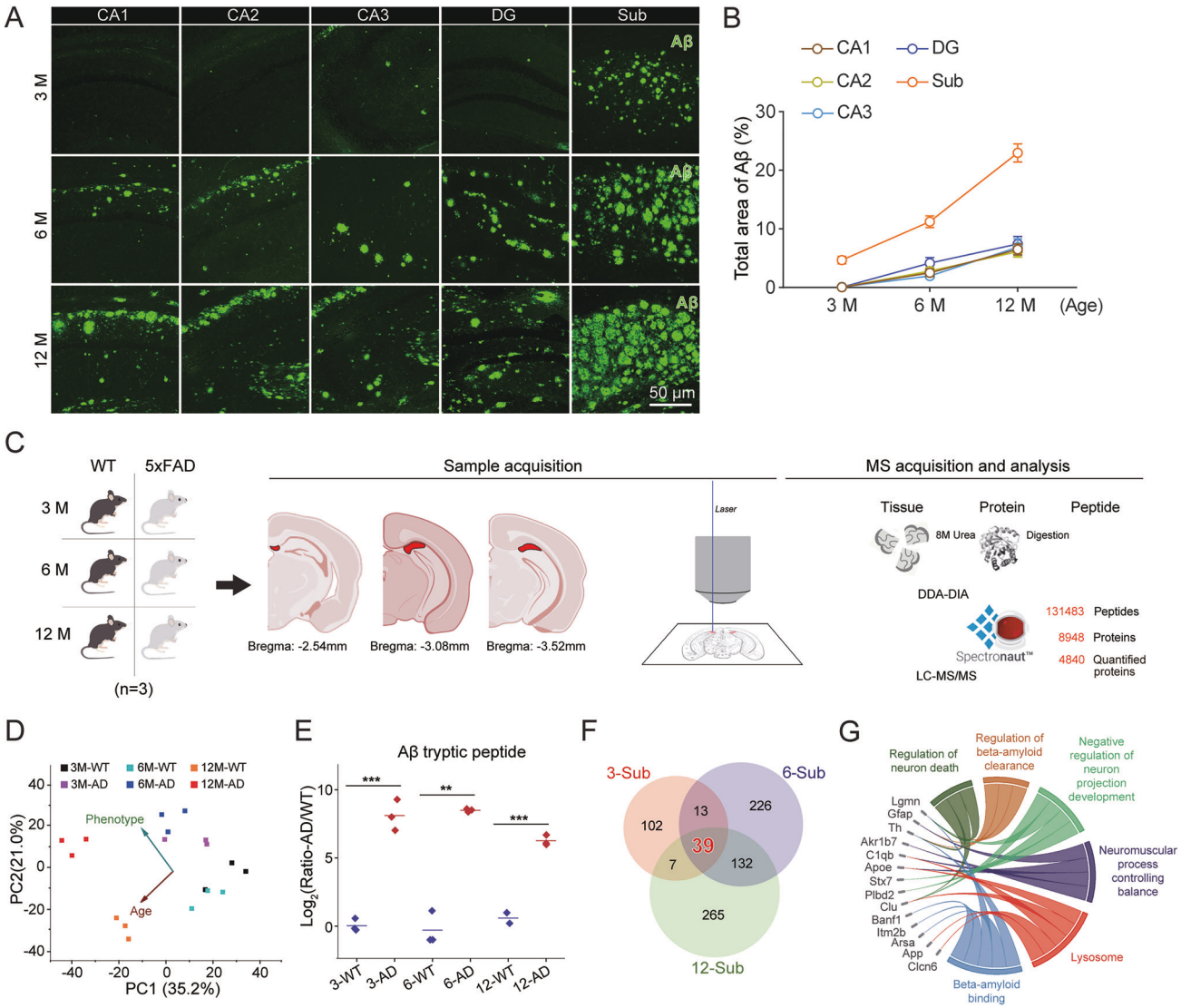

Fig. 1 Proteomic profiling of the subiculum during AD progression in 5×FAD mice. A Representative coronal images showing Aβ deposition in hippocampal subregions (CA1, CA2, CA3, DG, and subiculum) from 5×FAD mice at 3, 6, and 12 months of age. **B** Line graph illustrating the progressive increase in Aβ deposition across hippocampal subregions with age. Data represent 9 slices from 4 mice. **C** Schematic workflow depicting sample acquisition, laser microdissection, and MS analysis (n = 3 per group). **D** PCA of subiculum proteomes from all samples, showing separation by age and phenotype (WT vs AD). **E** Relative levels of the Aβ tryptic peptide in each group, normalized to WT controls. **F** Venn diagram showing significantly differentially expressed proteins (DEPs, fold change >1.2 or <0.83, $p < 0.05$) in 3-, 6-, and 12-month-old AD groups (n = 3 samples per group). **G** GO enrichment analysis of the 39 overlapping DEPs across all age groups, with connections between proteins and enriched biological processes. All data are represented as mean ± SEM. $^{**}p < 0.01$; $^{***}p < 0.001$.

neurons in the subiculum (Fig. S3A–C). Next, we investigated the role of these interneuron subtypes in Aβ pathology by selectively ablating PV, SST, or VIP interneurons in 3-month-old 5×FAD mice through targeted viral delivery of AAV-Cre and AAV-DIO-taCaspase3 to induce cell-specific apoptosis (Fig. 3A–C). Notably, only the ablation of PV-INs led to a significant reduction in Aβ plaque burden in the subiculum, while SST or VIP interneurons ablation had no effect (Fig. 3D, E). This indicates that PV-INs specifically drive the early accumulation of Aβ in the subiculum during AD progression. Interestingly, despite the early impact of PV-INs ablation on Aβ pathology, the density of PV-INs in the subiculum remained unchanged at 3 and 6 months of age but showed a significant reduction by 12 months in 5×FAD mice (Fig. S3D, E), suggesting a progressive loss of these interneurons as the disease advances. Compared to other hippocampal subregions, the highest density of PV-INs was observed in the subiculum (Fig. S4), aligning with the pattern of Aβ deposition across hippocampal subregions.

To further explore the functional role of PV-INs in AD pathology, we generated PV-Cre;5×FAD mice, allowing us to manipulate PV-INs specifically within the context of AD. These mice showed no difference in overall Aβ plaque count compared to 5×FAD littermates (Fig. S5A, B). Next, we explored whether early-stage Aβ pathology affects PV-INs activity. Whole-cell patch-clamp recordings from subicular PV-INs in these mice revealed that PV-INs were hyperactive during the early stages of AD, exhibiting depolarized resting membrane potentials and increased firing rates compared to control mice (Fig. 3F–J). This hyperactivity was accompanied by enhanced inhibitory input to pyramidal neurons, as evidenced by increased the amplitudes of spontaneous inhibitory postsynaptic currents (sIPSCs)

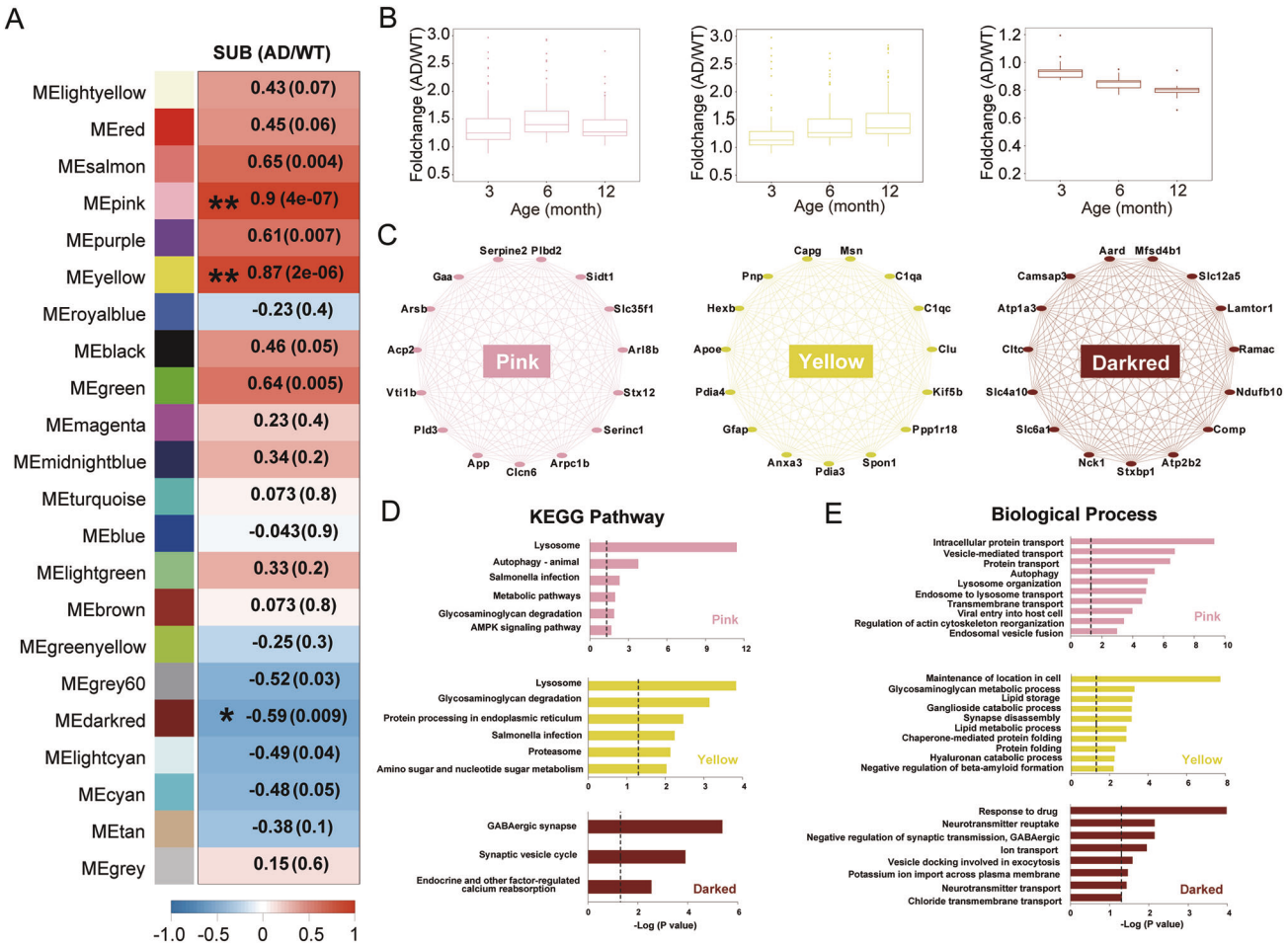

Fig. 2 Identification of protein co-expression modules associated with the AD phenotype through WGCNA. A Heatmap showing the correlation between module eigengenes (MEs) and AD compared to WT conditions. Positive correlations are shown in red, and negative correlations in blue, with p values indicated in parentheses. **B** Box plots showing fold changes (AD/WT) for the pink, yellow, and darkred modules at 3, 6, and 12 months. The median AD/WT ratio is indicated by the center line. **C** Network diagrams displaying proteins with high intramodular connectivity in the pink, yellow, and darkred modules. **D** KEGG pathway enrichment analysis of the pink, yellow, and darkred modules, highlighting key pathways related to lysosomal function, metabolic processes, and synaptic regulation. **E** Gene Ontology (GO) biological process enrichment analysis for the pink, yellow, and darkred modules, identifying significant processes such as protein transport, synaptic transmission, and lysosomal activity.

in PV-Cre;5×FAD mice (Fig. S5C, D), though no significant changes were observed in spontaneous excitatory postsynaptic currents (sEPSCs) (Fig. S5E, F). These results demonstrate that the early hyperactivation of PV-INs disrupts the inhibitory-excitatory balance in the subiculum, driving early pathological changes.

To assess whether eliminating hyperactive PV-INs could mitigate cognitive deficits, we selectively ablated PV-INs in the subiculum of 3-month-old PV-Cre;5×FAD mice and tested their spatial learning and memory performance three months later using the Morris water maze (MWM) (Fig. S5G). Mice with PV-INs ablation showed significantly improved performance, with shorter escape latencies and increased time spent in the target quadrant, compared to control virus-injected PV-Cre;5×FAD mice (Fig. S5H–L). These results indicate that eliminating hyperactive PV-INs can reverse cognitive deficits in AD mice. Remarkably, 3 months after PV-INs ablation, we observed a reduction in Aβ plaques not only in the subiculum but also across other brain regions, suggesting that PV-INs in the subiculum may influence the spread of Aβ pathology throughout the brain (Fig. S6A, B).

In summary, our findings demonstrate that PV-INs in the subiculum become hyperactive early in AD and contribute to both Aβ pathology and cognitive deficits. Targeted elimination of these hyperactive PV-INs can reduce Aβ deposition and restore cognitive function, positioning PV-INs as key regulators of early AD progression.

Chemogenetic inhibition of subicular PV-INs reduces Aβ pathology and improves memory performance

To further confirm the causal role of subicular PV interneuron hyperactivity in driving Aβ pathology, we used a chemogenetic approach to inhibit PV-IN activity in PV-Cre;5×FAD mice. AAV9-DIO-hM4Di-EYFP or control AAV9-DIO-EYFP virus was bilaterally injected into the subiculum at 10 weeks of age (Fig. 4A), followed by intraperitoneal administration of CNO (1 mg/kg daily) from 12 to 24 weeks of age (Fig. 4B). In the Morris water maze (MWM), 5×FAD mice with hM4Di activation displayed significantly improved spatial and memory compared to control 5×FAD mice, as reflected by reduced escape latency, increased time in the target zone, and increased platform crossings during probe trials, without affecting swim speed (Fig. 4C–G). Immunohistochemistry confirmed effective inhibition of PV-INs as evidenced by reduced c-fos expression and significant reduction of Aβ deposition in the subiculum (Fig. 4H, I). These findings suggest that chemogenetic inhibition of PV-IN hyperactivity attenuates Aβ pathology and improves cognitive function.

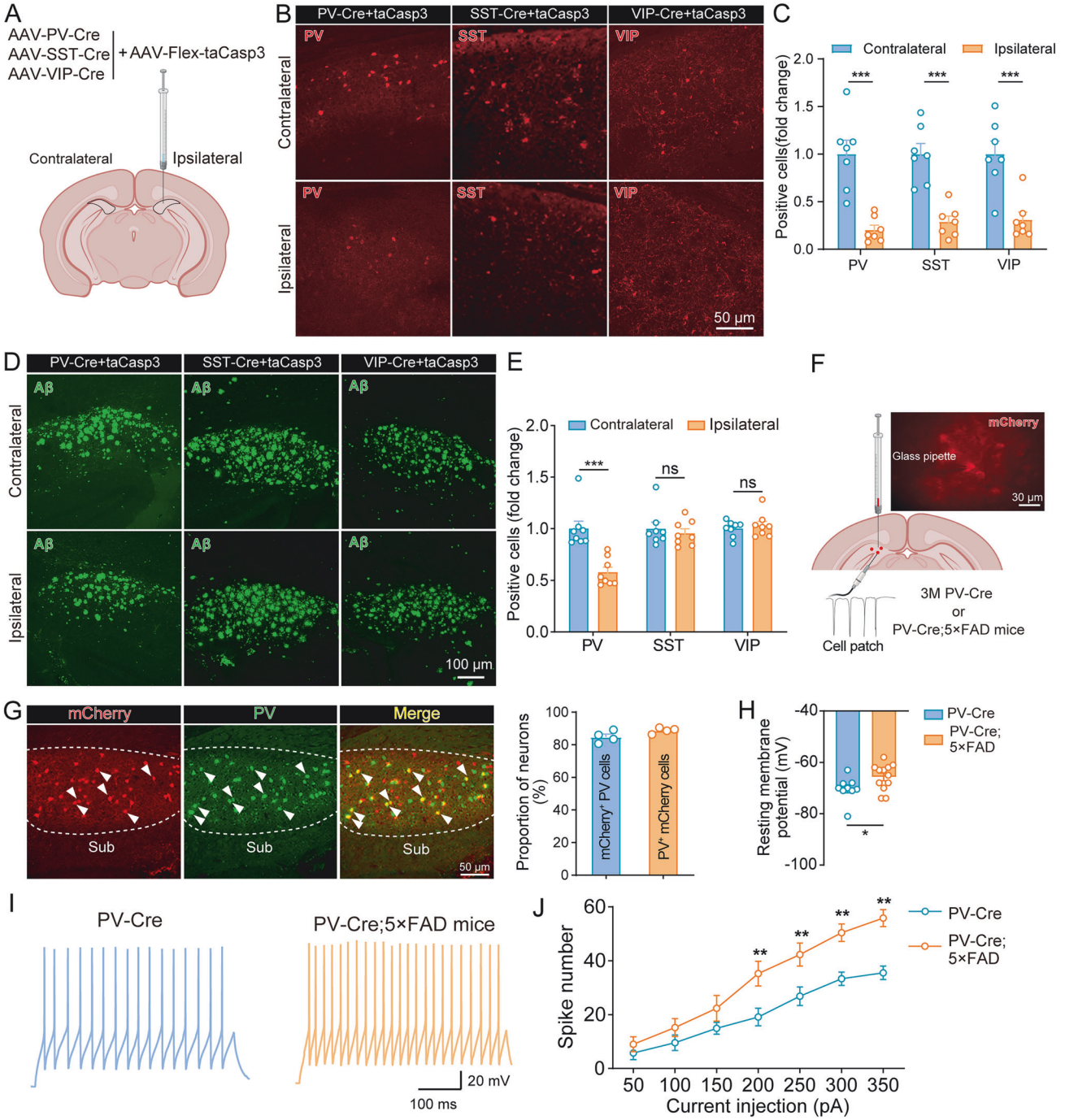

Fig. 3 Early ablation of subicular PV-INs reduces Aβ deposition and reveals PV-IN hyperactivity in 5×FAD mice. A Schematic representation of unilateral AAV injections into the subiculum of 3-month-old 5×FAD mice. Mice were injected with a mixture of either AAV-PV-Cre, AAV-SST-Cre, or AAV-VIP-Cre combined with AAV-EF1α-taCasp3-TEVp to selectively ablate PV, SST, or VIP interneurons. **B** Representative confocal images of PV, SST, and VIP immunostaining in the subiculum. **C** Quantification of the number of PV, SST, and VIP interneurons on the ipsilateral and contralateral sides of the subiculum (n = 7 slices from 3–4 mice per group, unpaired t-test). **D** Representative images of Aβ staining in the subiculum of 5×FAD mice after selective ablation of PV, SST, or VIP interneurons. **E** Quantification of Aβ plaque number in the subiculum after selective ablation of PV, SST, or VIP interneurons (n = 8 slices from 4 mice per group, unpaired t-test). **F** Schematic diagram showing mCherry labeling of PV-INs in the subiculum of PV-Cre or PV-Cre;5×FAD mice. **G** Representative images showing mCherry expression (red) and PV immunostaining (green) in the subiculum. Arrowheads point to mCherry and PV double-positive neurons. Quantification of the proportion of mCherry$^+$ and PV$^+$ cells is shown in the right panel (n = 4 mice per group). **H** Resting membrane potential of PV-INs is significantly depolarized in PV-Cre;5×FAD mice at 3 months of age compared to PV-Cre controls (n = 9 neurons/3 mice in PV-Cre mice and n = 12 neurons/4 mice in PV-Cre;5×FAD mice, unpaired t-test). **I** Representative voltage traces from PV-INs in PV-Cre and PV-Cre;5×FAD mice in response to 1-second current steps. **J** Quantification of spike number in response to depolarizing current injections (50–350 pA) in the two groups (n = 10 neurons from 3 mice per group, two-way ANOVA with the Holm-Sidak post hoc test). All data are represented as mean ± SEM. ns not significant, *p < 0.05, **p < 0.01, ***p < 0.001.

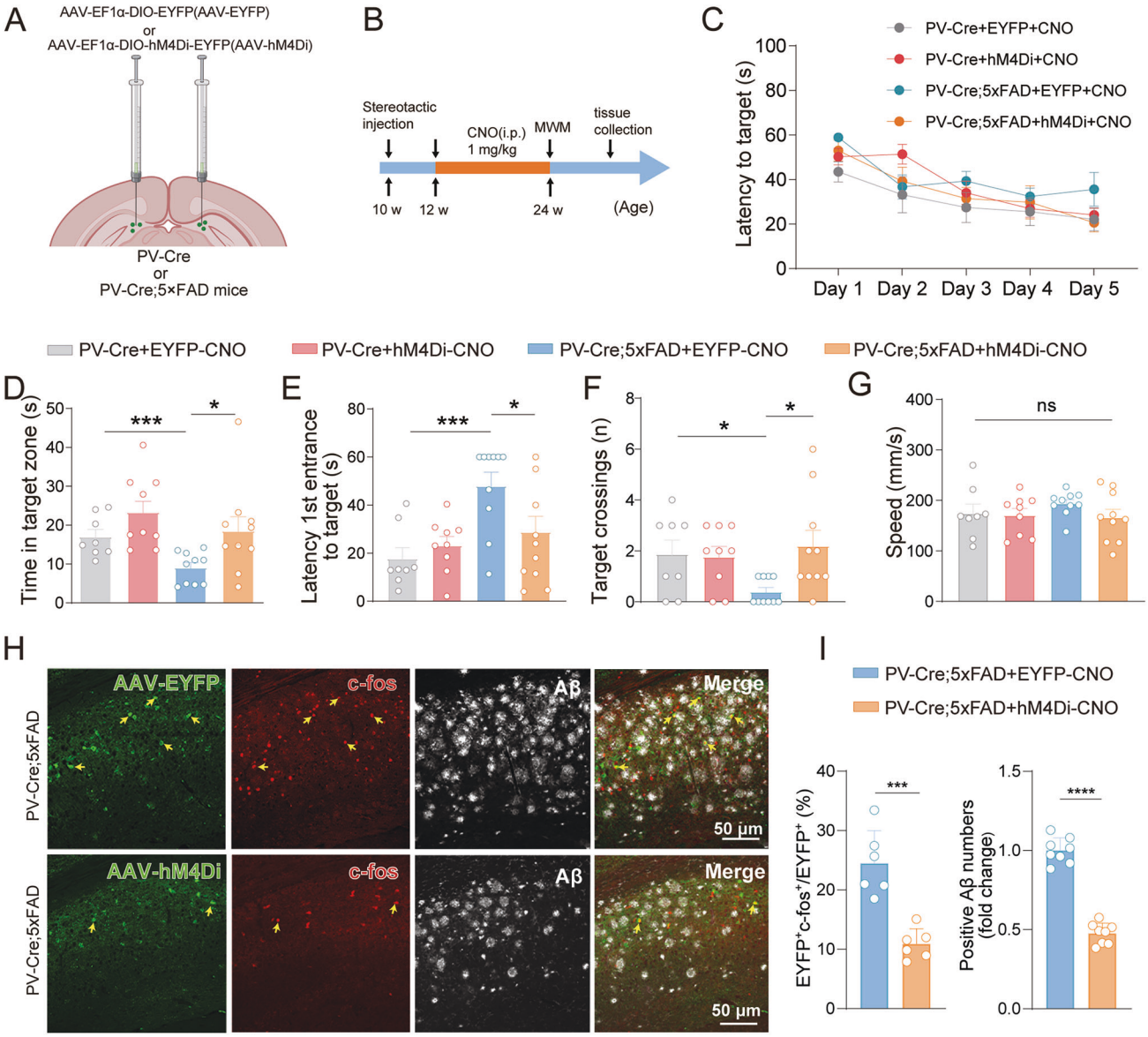

Fig. 4 Chemogenetic inhibition of subicular PV-INs improves spatial memory and reduces Aβ pathology in 5×FAD mice. A, **B** Schematic representation of bilateral injections for chemogenetic inhibition of subicular PV-INs in PV-Cre;5×FAD mice A and the timeline of the behavioral experiments B. **C** Spatial learning was assessed during the MWM over five consecutive training days (n = 8–10 mice in the four groups, respectively. Two-way ANOVA). **D**-**G** In the probe trial, the time spent in the target quadrant D, the latency to the platform E, the number of platform crossings F, and the average swim speed G were recorded and analyzed to assess memory retention and motor function in the four groups (n = 8–10 mice in the four groups, respectively. Two-way ANOVA). **H**, **I** Representative coronal images showing virus expression, c-fos, and Aβ immunohistostaining in the subiculum following hM4Di activation H. Yellow arrows indicate co-localization of AAV-infected cells and c-fos expression. Quantification of c-fos-positive and Aβ-positive cells I (n = 6–8 slices from 3–4 mice per group, unpaired t-test). All data are represented as mean ± SEM. ns not significant, *p < 0.05, ***p < 0.001, ****p < 0.0001.

PV knockdown in the subiculum alleviates cognitive deficits and reduces local and distal Aβ pathology

Our previous research demonstrated that PV expression levels are closely related to PV-INs activity [20]. Therefore, we employed an shRNA-mediated approach to selectively knock down PV in the subiculum of PV-Cre;5×FAD mice. Mice were bilaterally injected with either AAV-DIO-PV-shRNA (AAV-shPV) to specifically reduce PV expression or AAV-DIO-non-targeting shRNA (AAV-shNT) as a control (Fig. 5A, B). PV knockdown led to a marked reduction in c-fos expression, confirming that reduced PV levels decrease neuronal activity in the subiculum (Fig. S6C, D). Mice with PV knockdown also displayed improved performance in the MWM, with shorter escape latencies and more time spent in the target zone, similar to the effects seen in chemogenetically inhibited mice (Fig. 5C–G). In parallel, PV knockdown significantly reduced Aβ plaques in the subiculum (Fig. 5H, I). These findings indicate that both chemogenetic inhibition and PV knockdown reduce PV-INs hyperactivity, which in turn mitigates Aβ pathology and improves cognitive performance in early AD.

Recent studies have highlighted the critical role of the subiculum in various cognitive functions, including visual contextual behaviors, with evidence showing its connections to the visual cortex and key regions like CA1 [8]. To investigate whether PV-INs manipulation in the subiculum affects Aβ pathology in connected brain regions, we examined Aβ deposition in the visual cortex of 5×FAD mice after subicular injections of AAV-taCaspase3, AAV-hM4Di, or AAV-shPV. Remarkably, all three interventions led to a significant reduction in Aβ density in the visual cortex

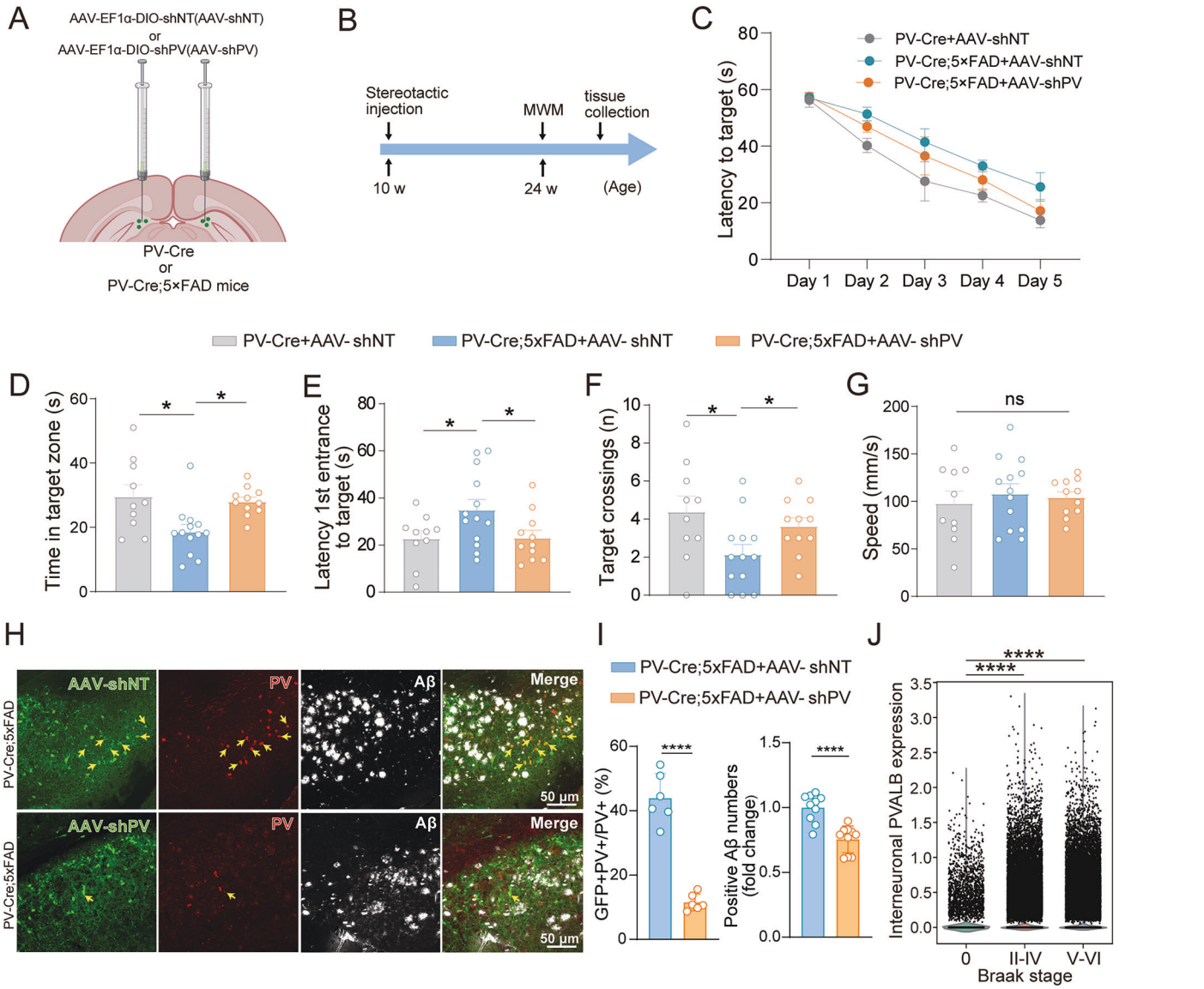

Fig. 5 PV knockdown phenocopies chemogenetic inhibition in reducing Aβ pathology and improving memory. A, **B** Schematic representation of bilateral AAV-DIO-shRNA injections for selective PV knockdown (AAV-shPV) in the subiculum of PV-Cre;5×FAD mice, with AAV-DIO-non-targeting shRNA (AAV-shNT) as a control A and the timeline of the behavioral experiments B. **C** Spatial learning in PV knockdown mice was assessed in the MWM over five training days (n = 10–13 mice in the three groups, two-way ANOVA with Tukey post hoc test). **D**-**G** Quantification of time spent in the target quadrant D, latency to first entrance to the platform zone E, number of target crossings F, and average swim speed G during the probe trial of the MWM (n = 10–13 mice in the three groups, one-way ANOVA with Tukey post hoc test). **H**, **I** Representative images showing PV knockdown in the subiculum and Aβ immunohistostaining H. Yellow arrows indicate co-localization of AAV-infected cells and PV-positive neurons. Quantification of PV-positive cells and Aβ-positive plaques I (n = 6–10 slices from 3–4 mice per group, unpaired t-test). **J** *PVALB* expression in GABAergic interneurons from patients across different Braak stages. Data are from 84 patients: 2 Braak 0 (12,107 neurons), 4 Braak II (16,721 neurons), 6 Braak III (23,985 neurons), 23 Braak IV (104,513 neurons), 34 Braak V (112,116 neurons), and 15 Braak VI (51,150 neurons). Data obtained from the SEA-AD dataset. All data are represented as mean ± SEM. ns not significant, *p < 0.05, ****p < 0.0001.

(Fig. S6E–J). These findings suggest that PV-INs in the subiculum not only regulate local pathology but may also influence Aβ propagation to distal regions, such as the visual cortex, underscoring the potential of PV-INs as therapeutic targets for reducing global brain pathology in AD.

To assess the relevance of PV-INs activity in the progression of AD in humans, we analyzed snRNA-seq data from the Seattle Alzheimer's Disease (SEA-AD) dataset. Specifically, we examined the expression of the *PVALB* gene, which encodes PV, in GABAergic interneurons from human brain samples at various Braak stages of AD. In samples from 84 individuals spanning Braak stages 0 to VI, *PVALB* expression was significantly elevated in interneurons from early to middle stages (Braak II-IV), peaking during these stages, and remaining elevated in later stages (Braak V-VI) compared to Braak 0 controls ($p < 0.0001$) (Fig. 5J). This suggests that PV-INs activity may play a prominent role in the early progression of AD.

In conclusion, our study reveals that subicular PV-INs are key regulators of early AD pathology. Inhibition of PV-INs hyperactivity significantly reduces Aβ burden and ameliorates cognitive deficits in 5×FAD mice, with beneficial effects extending to connected regions such as the visual cortex. Human AD data further highlight the importance of PV-INs activity in early disease stages, positioning these neurons as promising therapeutic targets for AD intervention.

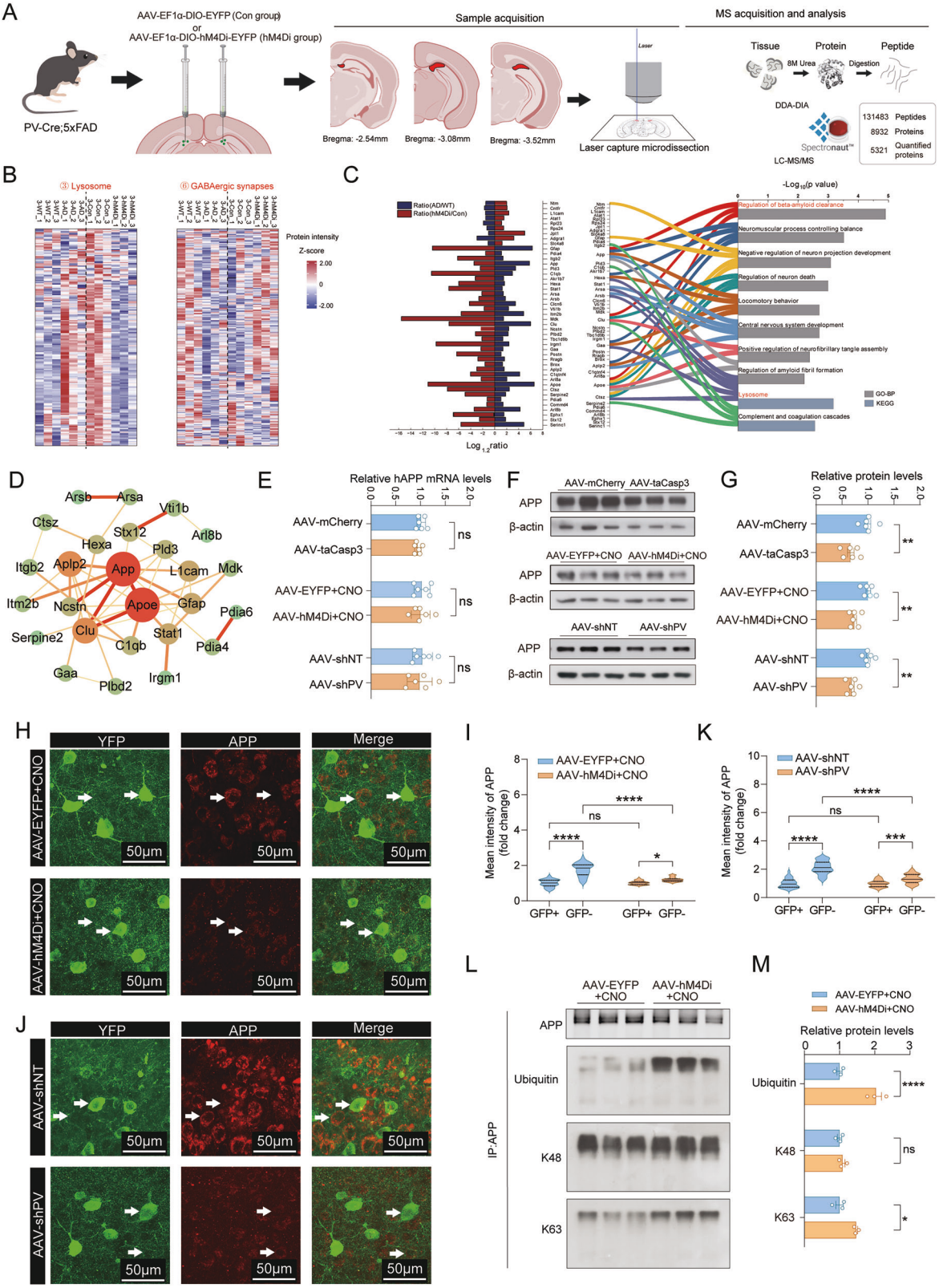

Inhibition of subicular PV interneurons restores inhibitory synaptic and lysosomal protein homeostasis and promotes APP degradation via K63-linked ubiquitination

To investigate the mechanisms behind the reduction in Aβ pathology following PV interneurons inhibition, we performed microdissection and quantitative proteomic analysis on the subiculum of 5×FAD mice injected bilaterally with either AAV-hM4Di or control AAV-EYFP to selectively inhibit PV-INs activity via chemogenetic methods (Fig. 6A and data file S3). A total of 5321 proteins were identified for quantification, with high-quality data

Fig. 6 Restoration of protein homeostasis in the subiculum of 5×FAD mice following PV interneuron inhibition, including enhanced GABAergic synapses, amelioration of lysosomal dysfunction, and reduced APP levels. A Schematic workflow depicting sample acquisition, laser microdissection, and mass spectrometry (MS) analysis (n = 3 per group). **B** Hierarchical clustering of DEPs related to lysosomes and GABAergic synapses across the four groups. **C** GO enrichment of DEPs showing opposite trends (fold change >1.2 or < 0.83, $p < 0.05$), highlighting pathways linked to Aβ metabolism and lysosomal function. **D** Protein-protein interaction network of DEPs, showing APP and APOE as central hubs. Node size reflects degree, edge width indicates interaction strength. **E** Quantification of human APP (hAPP) mRNA levels by RT-qPCR showing no significant change after AAV-taCasp3, AAV-hM4Di, or AAV-shPV injections (n = 6 mice/group, unpaired t-test). **F, G** Western blot analysis of APP in the subiculum following AAV-taCasp3, AAV-hM4Di, or AAV-shPV injections (n = 6 mice/group, unpaired t-test). **H, I** Representative images of YFP (AAV, green) and APP (red) in the subiculum, showing APP levels in YFP− and YFP+ cells after AAV-hM4Di injection (n = 27–30 cells from 3 mice, two-way ANOVA). **J, K** Representative images of YFP (AAV, green) and APP (red) in the subiculum, showing APP levels in YFP− and YFP+ cells after AAV-shPV injection (n = 34–35 cells from 3 mice, two-way ANOVA). **L, M** Immunoprecipitation (IP) of APP followed by Western blot showing total ubiquitination, K48- and K63-linked polyubiquitination of APP in AAV-EYFP and AAV-hM4Di groups after CNO treatment L. Quantification of APP-associated ubiquitin, K48-, and K63-linked ubiquitination levels normalized to IP-APP levels M (n = 3 mice/group, unpaired t-test). All data are represented as mean ± SEM. ns not significant, *$p < 0.05$, **$p < 0.01$, ****$p < 0.0001$.

confirmed by strong reproducibility across replicates (median CV < 12% and Pearson correlation coefficient = 0.97) (Fig. S7A–C and data file S3). Consistent with reduced Aβ pathology, peptides associated with Aβ were significantly lower in hM4Di-treated mice compared to controls (Fig. S7D).

Next, we investigated whether inhibiting PV interneurons activity could restore the dysregulated protein levels seen in AD brains. Specifically, we focused on lysosomal and GABAergic synapse-related proteins previously found dysregulated in the subiculum (Figs. 2 and S2). Our analysis showed that PV-INs inhibition restored these protein levels to near-normal (Fig. 6B). To identify proteins involved in modulating Aβ pathology, we compared DEPs between AD and WT brains and found 45 proteins with opposite trends between hM4Di-treated and control groups. GO enrichment analysis linked these proteins to Aβ metabolic processes, including pathways for Aβ clearance and fibril formation (Fig. 6C and data file S3). Protein interaction networks revealed that APP and ApoE were central to the network, both of which are well-established key proteins involved in Aβ metabolism, including its production, aggregation, and clearance (Fig. 6D). Western blotting confirmed a significant reduction in APP protein levels after PV-INs inhibition, while APP mRNA levels remained unchanged (Fig. 6E–G). Immunohistostaining further showed that APP reduction occurred in YFP-negative neurons, indicating that the effect on APP was not within PV-INs but rather surrounding neurons (Fig. 6H, I). PV knockdown similarly reduced APP in surrounding neurons, suggesting a consistent mechanism across different interventions (Fig. 6J, K). This reduction in APP was also observed in the visual cortex, a region connected to the subiculum, following both PV inhibition and knockdown, indicating that subicular PV-INs activity impacts broader cortical networks (Fig. S7E–H). Furthermore, we investigated the post-translational modification of APP and observed a significant increase in K63-linked polyubiquitination of APP following PV-INs inhibition (Fig. 6L, M). K63-linked ubiquitination is widely recognized to participate in endo-lysosomal trafficking and lysosome-associated degradation pathways [21]. This observation is consistent with the proteomic findings of reduced APP abundance and alleviated lysosomal dysfunction following PV-INs inhibition.

Moreover, PV interneurons inhibition led to increased GABAergic synapse-associated protein Gephyrin (Fig. S7I–L), while also reducing levels of the lysosomal accumulation around Aβ plaques, as indicated by decreased Lamp2-positive lysosomes (Fig. S7M–P). These findings align with proteomic data, showing that PV-INs inhibition alleviates lysosomal dysfunction and restores synaptic integrity in AD.

In summary, inhibition of subicular PV interneurons restores protein homeostasis by reducing lysosomal accumulation and APP levels while enhancing GABAergic synapses. The mechanism of APP degradation through K63-linked ubiquitination and lysosomal clearance plays a central role in these processes. These effects extend beyond the subiculum to broader cortical regions like the visual cortex, demonstrating the therapeutic potential of targeting PV interneurons in AD.

DISCUSSION

In this study, we demonstrate that subicular PV-INs are pivotal in driving early amyloid pathology in AD. Our findings reveal that hyperactivity of these neurons contributes to Aβ plaque accumulation in the subiculum, a region highly vulnerable to early AD pathology. Through targeted approaches such as PV-INs ablation, chemogenetic inhibition, and PV knockdown, we observed significant reductions in Aβ pathology and improvements in memory performance in 5×FAD mouse models. Notably, PV-INs inhibition also restored protein homeostasis by rebalancing GABAergic signaling, alleviating lysosomal dysfunction, and decreasing APP levels through a ubiquitination-associated pathway. Our results provide strong evidence that modulating subicular PV-INs activity may offer a promising strategy to slow both the pathological progression and cognitive decline in AD.

The protective effects of reducing PV-INs hyperactivity on Aβ pathology and cognitive function align with the broader hypothesis that neural hyperexcitability exacerbates the spread of AD pathology. Previous studies have shown that heightened neuronal activity can increase Aβ production via activity-dependent mechanisms, thereby accelerating Aβ aggregation [22–24]. In both AD patients and mouse models, Aβ tends to accumulate along circuits with aberrant neuronal activity, suggesting that network dysfunction is an early pathogenic driver [25, 26]. However, which specific neuronal subtypes are responsible for promoting this early pathology has remained unclear [27]. Emerging evidence indicates that in early AD, PV interneurons exhibit functional abnormalities such as hyperactivity or altered excitability, which may precede overt structural changes. This imbalance may result from multiple mechanisms, including metabolic stress, synaptic dysfunction, and altered calcium signaling. The dynamic relationship between PV neuron activity and density likely evolves throughout disease progression [28, 29]. Previous studies have primarily focused on PV-INs in the hippocampal CA1 region and prefrontal cortex (PFC), where they are critical for maintaining excitatory/inhibitory (E/I) balance and orchestrating network oscillations underlying cognition [30, 31]. However, the subiculum—an output hub of the hippocampus and an early site of Aβ deposition—has been relatively understudied in this context. Given its strategic anatomical position and vulnerability to early AD pathology, we hypothesized that PV-INs in the subiculum may act as key initiators of disease progression. We found that hyperactivity of subicular PV-INs likely disrupts E/I balance and serves as a trigger for early Aβ accumulation and cognitive impairment. This is consistent with other findings that inhibitory dysfunction often precedes excitatory hyperactivity and plaque deposition in AD mouse models [32, 33]. Our study

identifies PV-INs as critical initiators of early Aβ pathology in Alzheimer's disease, particularly within the subiculum. We demonstrate that hyperactivity of subicular PV-INs promotes local Aβ accumulation, while their inhibition or knockdown leads to a reduction in both local and distal plaque burden. Anatomically, the subiculum serves as a major hippocampal output hub, projecting to diverse cortical regions such as the entorhinal, retrosplenial, and visual cortices, providing a structural basis for broad circuit-level modulation [34]. These anatomical connections support the possibility that PV-INs may contribute not only to local Aβ production but also to the transneuronal propagation of Aβ pathology. Mechanistically, the modulation of neuronal activity is closely tied to Aβ generation and plaque vulnerability [35–37]. PV-INs, as key regulators of network oscillations, particularly gamma rhythms, exert strong control over excitatory output. Disruption of PV-IN function leads to aberrant gamma oscillations, which have been shown in mouse models to precede detectable Aβ or tau pathology and correlate with PV dysfunction [38, 39]. Causal studies further demonstrate that restoration or enhancement of gamma activity via optogenetics or sensory stimulation can reduce Aβ burden [40, 41], indicating a bidirectional relationship between gamma dynamics and Aβ pathology. Clinically, these findings may carry important translational implications. EEG-based studies in cognitively unimpaired individuals with positive Aβ or tau PET signals have reported abnormal gamma activity, including reduced power and impaired phase-amplitude coupling [42–44], suggesting that gamma rhythm alterations may serve as noninvasive, scalable biomarkers for early or even preclinical stages of AD. Our work thus not only implicates subicular PV-INs in early Aβ pathology but also connects them to functional biomarkers and circuit-based therapeutic strategies.

Our data indicate that targeting PV-INs hyperactivity reduces both local and distant Aβ pathology, suggesting a broader role for the subiculum in modulating amyloid spread to connected brain regions. This is in line with previous studies that have shown that the subiculum, as a hub within the hippocampal formation [45], is highly interconnected with other regions and plays a role in facilitating the propagation of pathological signals [15, 46, 47]. As the subiculum plays essential roles in cognitive functions such as spatial navigation and working memory [34, 48, 49], early Aβ accumulation here may initiate cognitive decline. The reduction of Aβ pathology in connected areas, such as the visual cortex, after PV neuron modulation suggests that the subiculum may serve as a hub for the propagation of AD pathology throughout the brain. These findings emphasize the therapeutic potential of subicular PV-INs as intervention points to mitigate both local and network-wide pathology.

Our proteomic analysis provides deeper insights into the molecular mechanisms underlying the reduction in Aβ pathology following PV-INs inhibition. We observed that APP levels were significantly reduced following PV-INs inhibition, concurrent with an increase in K63-linked polyubiquitination of APP—a post-translational modification implicated in endo-lysosomal trafficking and lysosome-associated degradation pathways. Importantly, the reduction in APP occurred in non-PV neurons, suggesting that PV-INs influence broader neural networks, potentially modulating APP expression through synaptic or circuit-level interactions. In addition, we identified APOE, a key protein involved in Aβ aggregation and clearance [50], as another central node affected by PV-INs inhibition. This suggests that PV-INs hyperactivity may modulate Aβ metabolism through multiple pathways, influencing both the production and clearance of Aβ. The precise mechanisms by which PV-INs regulate APP and APOE in surrounding cells remain to be clarified. One possibility is that hyperactive PV-INs disrupt network homeostasis, leading to compensatory changes in excitatory neurons or glial cells, which in turn modulate ubiquitination-mediated APP degradation and Aβ clearance. Although our study did not directly assess glial function, microglia—the brain's resident immune cells—are known to clear Aβ, and increasing evidence suggests that inhibitory neurons, including PV-INs, can modulate microglial activation [40]. Future studies should explore whether subicular PV-INs indirectly influence Aβ clearance via microglia, particularly by regulating APOE expression and lysosomal activity in glial cells.

In conclusion, our study establishes subicular PV-INs as critical regulators of early Aβ pathology and cognitive decline in AD. Targeting PV-IN hyperactivity not only reduces Aβ deposition locally and in distant brain regions but also restores synaptic and lysosomal homeostasis. These findings position subicular PV-INs as promising targets for early intervention in AD, with potential relevance to both circuit-level therapies and biomarker development.

MATERIALS AND METHODS

Ethics statement

All experimental procedures involving animals were approved by the Ethics Committee of Xiamen University for Animal Use in Research, and all methods were performed in accordance with the relevant guidelines and regulations.

Animals

Transgenic mice with 5 familial AD mutations (5×FAD) (JAX#034840) and parvalbumin (PV)-Cre mice (Jax#008069) used in this study were purchased from The Jackson Laboratory (Bar Harbor, ME). The animals were housed in a controlled environment (temperature: 23 ± 1 °C; 12 h light/dark cycle) with ad libitum access to food and water. Hemizygous 5×FAD mice were crossed with heterozygous PV-Cre mice, generating offspring that were heterozygous for Cre and positive for 5×FAD (PV-Cre;5×FAD), as well as Cre-positive non-5×FAD (PV-Cre) and WT littermate controls. PV-Cre;5×FAD transgenic mice and their age-matched PV-Cre littermates were used at 3 months of age for immunohistochemical analysis. This age was selected because preliminary characterization indicated that Aβ plaque deposition was already evident. To minimize variation and ensure consistent experimental conditions, only male mice were used in this study. 3-month-old litter/age-matched mice were randomly assigned to experimental groups and all the experiments were performed double-blinded. Animals were used according to "3Rs" principles (Replacement, Reduction and Refinement) in all experimental procedures. Behavioral experiments related to cognition were conducted at 6 months of age. Additionally, Gad2-Cre; Ai14 mice, which express tdTomato in Gad2-positive neurons, were generated by crossing Ai14 mice (JAX#007914) with Gad2-IRES-Cre mice (JAX#010802). Adult mice (P90) from this lineage were also used for immunohistochemical staining. Sample sizes were determined based on previous animal studies to ensure adequate power to detect significant differences ($p < 0.05$) [51].

Brain stereotaxic injection of AAV

The brain stereotaxic injection procedures were performed as follows. Mice were deeply anesthetized with sodium pentobarbital (40 mg/kg, i.p) and secured in a stereotaxic frame (RWD Life Science Co., Guangzhou, China). After shaving and making a midline incision to expose the skull, a small hole was drilled at the appropriate coordinates. A glass micropipette connected to a microsyringe (5 μL, Hamilton, NV, USA) was used to inject the virus into the subiculum at coordinates AP: −3.18 mm, ML: ±1.94 mm, DV: +1.72 mm. The injection rate was 0.1 μL/10 min. To minimize diffusion, the needle was kept in place for 15 min before being withdrawn, and the incision was then sutured. Mice were placed on a heating pad until fully recovered from anesthesia and allowed to survive for at least 3 weeks before subsequent analyses. Recombinant adeno-associated viral (AAV) vectors were used to deliver target genes. The following AAV constructs were purchased from BrainVTA (BrainVTA Co., Ltd., Wuhan, China): AAV9-EF1α-DIO-EYFP (5.17×10^{12} vg/mL), AAV9-EF1α-DIO-hM4Di-EYFP (4.09×10^{12} vg/mL), AAV9-EF1α-flex-mCherry (2.0×10^{12} vg/mL), AAV9-EF1α-flex-taCasp3-TEVp-WPRE-pA (2.48×10^{12} vg/mL), AAV9-hSyn-DIO-mCherry (4.72×10^{12} vg/mL), AAV9-PV-Cre (3.01×10^{12} vg/mL). AAV9-fSST-Cre (4.58×10^{12} vg/mL) and AAV9-VIP-Cre (5.62×10^{12} vg/mL) were obtained from Taitool Bioscience (Shanghai, China). To evaluate the role of subicular PV neurons in the development of Aβ plaques, 200 nL of AAV9-EF1α-flex-taCasp3-TEVp-WPRE-pA was unilaterally injected into the subiculum of PV-Cre;5×FAD mice. For behavioral testing, bilateral injections were performed. To investigate the involvement of subicular PV neurons, SST neurons and VIP neurons in Aβ deposition, a 1:1 mixture of AAV9-PV/fSST/VIP-Cre and AAV9-

EF1α-flex-taCasp3-TEVp-WPRE-pA (200 nL totally) was injected unilaterally into the subiculum of 5×FAD mice.

shRNA

To downregulate parvalbumin protein expression, we utilized AAV vectors generated and purified by BrainVTA (BrainVTA Co., Ltd., Wuhan, China). The shRNA sequence targeting parvalbumin was 5′-GCTGGATGCTTTGCTGAAAGA-3′. For parvalbumin knockdown in subiculum cells, we delivered 200 nL AAV-EF1α-DIO-EYFP-MIR30-shRNA (parvalbumin) (5.27×10^{12} vg/mL) or the control virus AAV-EF1α-DIO-EYFP-MIR30-shRNA (non-targeting, NT) (2.61×10^{12} vg/mL) into the subiculum region of 2–3-month-old PV-Cre;5×FAD mice. Approximately 1 month after the viral delivery, the mice were sacrificed, and brain tissues were collected for immunohistochemical analysis.

Chemogenetical manipulation of PV-INs

Mice received intraperitoneal injections of Clozapine-N-oxide (CNO, catalog #C0832, Sigma) dissolved in 0.9% sterile saline and 0.9% sterile saline as a control. After a 3-week period for the chemogenetic viral expression, mice were administered daily doses of CNO (1 mg/kg, targeting hM4Di receptors) for 12 weeks. Treatment was halted 48 h before conducting behavioral testing or immunohistochemical analysis.

Immunohistochemical staining and microscopy

All animals were deeply anesthetized with sodium pentobarbital (60 mg/kg, i.p.) and perfused intracardially with 30 mL of 0.01 M phosphate-buffered saline (PBS, pH 7.4), followed by 150 mL of 4% paraformaldehyde (PFA) in PBS. After perfusion, brains were quickly collected and stored in PBS-buffered 30% sucrose solution at 4 °C until the brain blocks sunk to the bottom of the containers. For whole-brain quantitative mapping, the blocks were serially sectioned into 30-μm-thick coronal slices at 10 bregma levels: 2.2, 1.7, 0.9, 0.5, −0.4, −1.0, −1.7, −3.1, and −5.4 mm (including the subiculum and visual cortex), using a freezing microtome (CM1950, Leica, Heidelberg, Germany). Sections were collected in six sets, with each dish containing every sixth serial section.

For immunofluorescence, 30-μm coronal sections were pretreated with 0.3% Triton X-100 for 5 min at room temperature, blocked with 10% goat serum in PBS for 1 h, and incubated overnight at 4 °C with primary antibodies. The following day, the tissue was rinsed in PBS, incubated with secondary antibodies for 1 h at room temperature, and rinsed again. Mounted sections were visualized and imaged using an epifluorescence microscope (FV1000MPE-B, Olympus, Tokyo, Japan).

Primary antibodies used for immunostaining were: anti-PV (rabbit, 1:1000; Abcam, ab181086), anti-Aβ (MOAB-2, mouse, 1:1000; Abcam, ab126649), anti-SST (rat, 1:500; Millipore, MAB354), anti-c-fos (rabbit, 1:500; CST, 2250 s), anti-VIP (rabbit, 1:500; Abcam, ab22736), anti-APP (rabbit, 1:500, abcam, ab241592), Thioflavin S (1:1000, sigma, T3516). Alexa Fluor 594/488 donkey anti-mouse/rabbit secondary antibodies and Mounting Medium with DAPI were obtained from Invitrogen.

Western blotting

Western blot analyses were conducted as described in previous study [52]. Subiculum and visual cortex tissues from at least three pairs of control and AAV-treated male mice were collected for protein extraction. Briefly, tissue samples were manually homogenized in five volumes of suspension buffer containing 0.1 M NaCl, 0.01 M Tris–Cl (pH 7.6), 0.001 M EDTA (pH 8), 1 μg/mL aprotinin, 100 μg/mL phenylmethylsulfonyl fluoride, and 1% SDS. Samples were heated at 95 °C for 10 min, centrifuged, and the supernatant was collected. Proteins were separated on 8% polyacrylamide gels at 80 V for 120 min and transferred to a PVDF membrane (Millipore; Immobilon-P) at 300 mA for 70 min. Blots were incubated with primary antibodies, including SC-348 at a 1:100 dilution, and immunoreactivity was detected using chemiluminescence. Target protein levels were normalized to β-actin levels and expressed as fold changes relative to controls. Primary antibodies used were as follows: anti-APP (rabbit, 1:2000; SGB, D260097-0025), and anti-β-actin (mouse, 1:2000; Proteintech, 66009-1-Ig). Secondary antibodies, goat anti-rabbit IgG (H + L)-HRP and goat anti-mouse IgG (H + L)-HRP, were obtained from Millipore (#AP132P, #AP124P).

Behavioral assays

Morris water maze (MWM). Cognitive behaviors were assessed using the Morris Water Maze (MWM) as described previously, with slight modifications [53]. In brief, spatial memory was tested in a circular water tank (120 cm in diameter) filled with tap water maintained at 22 ± 2 °C. Spatial reference cues in the form of different shapes were placed on the walls around the maze. A camera mounted above the maze recorded the swimming paths of the mice. During acquisition trials, a platform submerged 1–2 cm below the water surface served as the escape target. Mice were released from one of four starting points (N, S, E, W) and allowed 60 seconds to locate the hidden platform. If unsuccessful, they were gently guided to the platform and remained there for at least 10 seconds. Each mouse underwent four trials per day, with a minimum inter-trial interval of 1 h. Escape latency, representing spatial learning and memory acquisition, was recorded for each trial. On day 5, a probe test was conducted by removing the platform. In this probe trial, the time spent in each quadrant of the maze was measured, with the focus on the target quadrant where the platform was previously located. Performance was evaluated based on escape latency during training trials and the amount of time spent in the target quadrant during the probe trial, which indicated memory retention.

Electrophysiological recording

For brain slice preparations, mice were deeply anesthetized with isoflurane, and 300-μm-thick coronal brain sections containing the subiculum were cut at 4 °C using a vibratome (Leica LS1200s) in oxygenated artificial cerebrospinal fluid (ACSF). The ACSF composition was (in mM): 124 NaCl, 2.5 KCl, 2 $MgSO_4$, 2 $CaCl_2$, 25 $NaHCO_3$, 1 NaH_2PO_4, and 37 glucose, with a pH of 7.4. The brain slices were transferred to a recording chamber maintained with oxygenated ACSF at 32 °C for 30 min, then equilibrated at room temperature (RT). Pyramidal neurons in the subiculum of PV-Cre and PV-Cre;5×FAD mice were selected for recording. The recordings were conducted in a submerged recording chamber perfused with oxygenated ACSF (95% O_2, 5% CO_2) at RT at a rate of 1–1.5 mL/min. The ACSF composition for perfusion was (in mM): 126 NaCl, 2.5 KCl, 1.2 NaH_2PO_4, 2.4 $MgCl_2{\cdot}6H_2O$, 1.2 $CaCl_2$, 18 $NaHCO_3$, and 11 glucose. Patch pipettes (5–8 MΩ) were filled with an intracellular solution containing (in mM): 140 $CsCH_3SO_3$, 2 $MgCl_2{\cdot}6H_2O$, 5 TEA-Cl, 10 HEPES, 2.5 MgATP, 0.3 Na_2GTP, and 1 EGTA, adjusted to pH 7.2–7.4 with CsOH. Spontaneous excitatory postsynaptic currents (sEPSCs) were recorded at a holding potential of −70 mV, and spontaneous inhibitory postsynaptic currents (sIPSCs) were recorded at 0 mV. To assess the relationship between spike number and the intensity of injected currents, PV neurons were current-clamped and injected with depolarizing currents ranging from 50 to 350 pA in 50 pA steps. The rheobase current (the minimum current required to elicit an action potential) was determined by injecting depolarizing currents in 2 pA steps. Recordings were performed using a MultiClamp 700B amplifier (Axon Instruments, Sunnyvale, CA, USA), digitized at 5 kHz by DigiData 1550B (Axon Instruments). The access resistance (10–30 MΩ) was monitored throughout the experiments, and recordings were discarded if the access resistance changed by more than 15% during the experiment.

Proteomic sample preparation

Subiculum tissues (300 μm thick) were microdissected from WT and 5×FAD mice using a Leica LMD7, as previously described [54]. The tissues were lysed with lysis buffer (8 M urea, 50 mM ammonium bicarbonate (ABC), 1% protease inhibitor, 1% phosphatase inhibitor) and subjected to ultra-sonication (Scientz-IID, China) in an ice bath. After centrifugation (16000×g, 20 min, 4 °C), supernatants were collected, and protein concentrations were determined using a BCA assay. Approximately 30 μg of protein per sample was used for LC-MS/MS analysis. Protein reduction was performed with 25 mM dithiothreitol (DTT) for 1 h at 56 °C, followed by alkylation with 50 mM iodoacetamide (IAA) for 30 min in the dark. Proteins were digested using the filter-aided sample preparation (FASP) method with trypsin (1:50, trypsin: protein) at 37 °C for 12–16 h, and peptides were lyophilized.

For library generation, 1/4 of the peptides from each group were subjected to high pH reverse-phase fractionation on an Agilent 1290 HPLC system equipped with a Durashell C18 column. Two mobile phases (A: H_2O with $NH3{\cdot}H_2O$ (pH 10), B: 80% ACN with $NH3{\cdot}H_2O$ (pH 10)) were applied with a 75 min gradient at 0.3 mL/min. Fractions were collected every minute from 10–75 min, resulting in 22 combined fractions.

Peptide fractions were analyzed using an Easy-nLC 1200 system coupled with an Orbitrap Fusion Lumos mass spectrometer. The capillary column (150 μm i.d. × 15 cm) was packed in-house with 1.9 μm Venusil XBP C18 silica particles. Mobile phases consisted of (A) 2% ACN with 0.1% formic acid (FA) and (B) 98% ACN with 0.1% FA. The separation gradient was 160 min at a flow rate of 600 nL/min. The spray voltage was 2400 V,

and the ion transfer tube was set to 320 °C. MS1 spectra were acquired from m/z 350–1200 with a resolution of 60,000, followed by MS/MS spectra acquisition using HCD with 30% collision energy and a resolution of 15,000. The isolation window was set to 1.6 m/z with a 3 s cycle time and a 45 s dynamic exclusion.

DIA analysis was performed on peptides from each group under the same conditions. MS1 was conducted as above, while targeted MS/MS scans were acquired at 30,000 resolution with HCD at 35% collision energy. DIA was performed using 60 variable isolation windows, each overlapping by 1 m/z.

Proteomic data analysis

Mass spectrometry (MS) data from the 22 DDA fractions were analyzed using Proteome Discoverer (PD, Thermo, version 2.5.0.4.00), with searches conducted against the Uniprot Mus musculus Swiss-Prot database (downloaded on 05/19/2022, 17,102 proteins), supplemented with mutated human APP and PSEN1 gene sequences. Spectral library generation and quantification of the subiculum groups were performed using Spectronaut™ 14.0 (Biognosys). PD search results, along with the FASTA file, were imported into Spectronaut to construct a spectral library, which was then used for DIA analysis. DIA data were processed with default parameters, including dynamic XIC extraction based on iRT calibration and gradient stability (correction factor 1). The precursor and protein Q-value cutoff was set to 1%. Protein quantification was performed using label-free quantification (LFQ) with automatic cross-run normalization enabled. Proteins identified in two or more biological replicates with a fold change >1.2 or < 0.83, and p-value < 0.05, were considered significantly differentially expressed. The mass spectrometric data generated in this study have been deposited to ProteomeXchange Consortium (https://proteomecentral.proteomexchange.org) via the iProX partner repository, and are publicly available as of the date of publication with the dataset identifier PXD056984.

Analysis of public snRNA-seq datasets (SEA-AD)

To reanalyze publicly available snRNA-seq datasets of human patients with Alzheimer's disease (AD) [55], we retrieved raw count matrices and associated metadata from the AD Knowledge Portal under accession number syn26273709 (SEA-AD). The dataset was processed and reanalyzed following previously established methods [56]. To assess PVALB expression in GABAergic interneurons across different Braak stages, we extracted GABAergic neuronal subpopulations from the dataset and visualized PVALB expression levels using violin plots. The dataset consists of single-nucleus transcriptomic profiles from 84 AD patients categorized by Braak stage: 2 Braak 0 (12,107 neurons), 4 Braak II (16,721 neurons), 6 Braak III (23,985 neurons), 23 Braak IV (104,513 neurons), 34 Braak V (112,116 neurons), and 15 Braak VI (51,150 neurons).

Data analysis and statistics

Weighted Gene Co-expression Network Analysis (WGCNA) was performed using protein expression values from the subiculum of AD and WT mice. A power of 16 was selected to build a scale-free topology based on the relationship between power and scale independence. Hybrid dynamic tree cutting was applied with a minimum module size of 30 genes and a merging threshold of 0.25. Each module was summarized by its eigengene (the first principal component of the scaled module expression profiles) and assigned a unique color identifier. Genes not meeting these criteria were assigned to the grey module. To assess module correlation with phenotype, WT was assigned 0 and AD was assigned 1. Modules significantly associated with phenotype were annotated using WGCNA R functions, and hub genes (connectivity ≥0.8) were identified. Cytoscape was used to visualize intramodular gene-gene connections.

Results are expressed as mean ± SEM. Statistical analyses between two groups were performed using Student's t-test (GraphPad Prism 7.0), and comparisons between multiple groups were made using one-way or repeated measures ANOVA, followed by LSD post-hoc tests. The analyzed sample sizes are indicated in the respective figure legends. P-values < 0.05 were considered statistically significant.

DATA AVAILABILITY

Materials and reagents used in this study are listed in the Materials and Methods section. Reagents generated in our laboratory in this study or previous studies are available upon reasonable request. Further information and requests for resources and reagents should be directed to and will be fulfilled by the lead contact, Jie Zhang (jiezhang@xmu.edu.cn). The mass spectrometric proteomics data generated in this study have been deposited in the ProteomeXchange Consortium (https://www.proteomexchange.org/) via the iProX partner repository and are publicly available as of the date of publication with the dataset identifier PXD056984.

REFERENCES

1. Guo T, Zhang D, Zeng Y, Huang TY, Xu H, Zhao Y. Molecular and cellular mechanisms underlying the pathogenesis of Alzheimer's disease. Mol Neurodegener. 2020;15:40.
2. Zhang Y, Chen H, Li R, Sterling K, Song W. Amyloid beta-based therapy for Alzheimer's disease: challenges, successes and future. Signal Transduct Target Ther. 2023;8:248.
3. Karran E, De Strooper B. The amyloid hypothesis in Alzheimer disease: new insights from new therapeutics. Nat Rev Drug Discov. 2022;21:306–18.
4. Zhang YW, Thompson R, Zhang H, Xu H. APP processing in Alzheimer's disease. Mol Brain. 2011;4:3.
5. Busche MA, Hyman BT. Synergy between amyloid-beta and tau in Alzheimer's disease. Nat Neurosci. 2020;23:1183–93.
6. Davies DC, Wilmott AC, Mann DM. Senile plaques are concentrated in the subicular region of the hippocampal formation in Alzheimer's disease. Neurosci Lett. 1988;94:228–33.
7. Schonheit B, Zarski R, Ohm TG. Spatial and temporal relationships between plaques and tangles in Alzheimer-pathology. Neurobiol Aging. 2004;25:697–711.
8. Sun Y, Jin S, Lin X, Chen L, Qiao X, Jiang L, et al. CA1-projecting subiculum neurons facilitate object-place learning. Nat Neurosci. 2019;22:1857–70.
9. Dunn AR, Neuner SM, Ding S, Hope KA, O'Connell KMS, Kaczorowski CC. Cell-type-specific changes in intrinsic excitability in the subiculum following learning and exposure to novel environmental contexts. eNeuro. 2019;5:ENEURO.0484-18.2018.
10. Carlesimo GA, Piras F, Orfei MD, Iorio M, Caltagirone C, Spalletta G. Atrophy of presubiculum and subiculum is the earliest hippocampal anatomical marker of Alzheimer's disease. Alzheimers Dement (Amst). 2015;1:24–32.
11. Rossler M, Zarski R, Bohl J, Ohm TG. Stage-dependent and sector-specific neuronal loss in hippocampus during Alzheimer's disease. Acta Neuropathol. 2002;103:363–9.
12. Trujillo-Estrada L, Davila JC, Sanchez-Mejias E, Sanchez-Varo R, Gomez-Arboledas A, Vizuete M, et al. Early neuronal loss and axonal/presynaptic damage is associated with accelerated amyloid-beta accumulation in AbetaPP/PS1 Alzheimer's disease mice subiculum. J Alzheimers Dis. 2014;42:521–41.
13. Tardif CL, Devenyi GA, Amaral RSC, Pelleieux S, Poirier J, Rosa-Neto P, et al. Regionally specific changes in the hippocampal circuitry accompany progression of cerebrospinal fluid biomarkers in preclinical Alzheimer's disease. Hum Brain Mapp. 2018;39:971–84.
14. Hijazi S, Smit AB, van Kesteren RE. Fast-spiking parvalbumin-positive interneurons in brain physiology and Alzheimer's disease. Mol Psychiatry. 2023;28:4954–67.
15. George S, Ronnback A, Gouras GK, Petit GH, Grueninger F, Winblad B, et al. Lesion of the subiculum reduces the spread of amyloid beta pathology to interconnected brain regions in a mouse model of Alzheimer's disease. Acta Neuropathol Commun. 2014;2:17.
16. Bates GP, Rodriguez GA, Barrett GM, Duff KE, Hussaini SA. Chemogenetic attenuation of neuronal activity in the entorhinal cortex reduces Aβ and tau pathology in the hippocampus. PLOS Biology. 2020;18:e3000851.
17. Abe Y, Ikegawa N, Yoshida K, Muramatsu K, Hattori S, Kawai K, et al. Behavioral and electrophysiological evidence for a neuroprotective role of aquaporin-4 in the 5×FAD transgenic mice model. Acta Neuropathologica Communications. 2020;8:67.
18. Kalxdorf M, Müller T, Stegle O, Krijgsveld J. IceR improves proteome coverage and data completeness in global and single-cell proteomics. Nature Communications. 2021;12:4787.
19. Li L, Sun C, Sun Y, Dong Z, Wu R, Sun X, et al. Spatially resolved proteomics via tissue expansion. Nature Communications. 2022;13:7242.
20. Leng L, Zhuang K, Lin H, Ding J, Yang S, Yuan Z, et al. Menin reduces parvalbumin expression and is required for the anti-depressant function of ketamine. Adv Sci (Weinh). 2024;11:e2305659.
21. Scavone F, Lian S, Eskelinen EL, Cohen RE, Yao T. Trafficking of K63-polyubiquitin-modified membrane proteins in a macroautophagy-independent pathway is linked to ATG9A. Mol Biol Cell. 2025;36:ar42.
22. Anastacio HTD, Matosin N, Ooi L. Neuronal hyperexcitability in Alzheimer's disease: what are the drivers behind this aberrant phenotype? Transl Psychiat. 2022;12:257.
23. Cirrito JR, Yamada KA, Finn MB, Sloviter RS, Bales KR, May PC, et al. Synaptic activity regulates interstitial fluid amyloid-β levels in vivo. Neuron. 2005;48:913–22.
24. Bero AW, Yan P, Roh JH, Cirrito JR, Stewart FR, Raichle ME, et al. Neuronal activity regulates the regional vulnerability to amyloid-β deposition. Nature Neuroscience. 2011;14:750–U353.

25. Buckner RL, Snyder AZ, Shannon BJ, LaRossa G, Sachs R, Fotenos AF, et al. Molecular, structural, and functional characterization of Alzheimer's disease: evidence for a relationship between default activity, amyloid, and memory. J Neurosci. 2005;25:7709–17.
26. Sperling RA, LaViolette PS, O'Keefe K, O'Brien J, Rentz DM, Pihlajamaki M, et al. Amyloid deposition is associated with impaired default network function in older persons without Dementia. Neuron. 2009;63:178–88.
27. Busche MA, Konnerth A. Neuronal hyperactivity-A key defect in Alzheimer's disease? Bioessays. 2015;37:624–32.
28. Lodge DJ, Behrens MM, Grace AA. A loss of parvalbumin-containing interneurons is associated with diminished oscillatory activity in an animal model of schizophrenia. J Neurosci. 2009;29:2344–54.
29. Dougherty SE, Hollimon JJ, McMeekin LJ, Bohannon AS, West AB, Lesort M, et al. Hyperactivity and cortical disinhibition in mice with restricted expression of mutant huntingtin to parvalbumin-positive cells. Neurobiology of disease. 2014;62:160–71.
30. Ge J, Xie S, Duan J, Tian B, Ren P, Hu E, et al. Imbalance between hippocampal projection cell and parvalbumin interneuron architecture increases epileptic susceptibility in mouse model of methyl CpG binding protein 2 duplication syndrome. Epilepsia. 2024;65:2483–96.
31. Hadler MD, Tzilivaki A, Schmitz D, Alle H, Geiger JRP. Gamma oscillation plasticity is mediated via parvalbumin interneurons. Science advances. 2024;10:eadj7427.
32. Verret L, Mann EO, Hang GB, Barth AMI, Cobos I, Ho K, et al. Inhibitory interneuron deficit links altered network activity and cognitive dysfunction in alzheimer model. Cell. 2012;149:708–21.
33. Palop JJ, Mucke L. Network abnormalities and interneuron dysfunction in Alzheimer disease. Nat Rev Neurosci. 2016;17:777–92.
34. O'Mara S. The subiculum: what it does, what it might do, and what neuroanatomy has yet to tell us. J Anat. 2005;207:271–82.
35. Bero AW, Yan P, Roh JH, Cirrito JR, Stewart FR, Raichle ME, et al. Neuronal activity regulates the regional vulnerability to amyloid-beta deposition. Nat Neurosci. 2011;14:750–6.
36. Kamenetz F, Tomita T, Hsieh H, Seabrook G, Borchelt D, Iwatsubo T, et al. APP processing and synaptic function. Neuron. 2003;37:925–37.
37. Cirrito JR, Yamada KA, Finn MB, Sloviter RS, Bales KR, May PC, et al. Synaptic activity regulates interstitial fluid amyloid-beta levels in vivo. Neuron. 2005;48:913–22.
38. Arroyo-Garcia LE, Isla AG, Andrade-Talavera Y, Balleza-Tapia H, Loera-Valencia R, Alvarez-Jimenez L, et al. Impaired spike-gamma coupling of area CA3 fast-spiking interneurons as the earliest functional impairment in the App(NL-G-F) mouse model of Alzheimer's disease. Mol Psychiatry. 2021;26:5557–67.
39. Ahnaou A, Moechars D, Raeymaekers L, Biermans R, Manyakov NV, Bottelbergs A, et al. Emergence of early alterations in network oscillations and functional connectivity in a tau seeding mouse model of Alzheimer's disease pathology. Sci Rep. 2017;7:14189.
40. Iaccarino HF, Singer AC, Martorell AJ, Rudenko A, Gao F, Gillingham TZ, et al. Gamma frequency entrainment attenuates amyloid load and modifies microglia. Nature. 2016;540:230–+.
41. Martorell AJ, Paulson AL, Suk HJ, Abdurrob F, Drummond GT, Guan W, et al. Multi-sensory gamma stimulation ameliorates Alzheimer's-associated pathology and improves cognition. Cell. 2019;177:256–71.e22.
42. Engels MM, Hillebrand A, van der Flier WM, Stam CJ, Scheltens P, van Straaten EC. Slowing of hippocampal activity correlates with cognitive decline in early onset Alzheimer's disease. An MEG Study with Virtual Electrodes. Front Hum Neurosci. 2016;10:238.
43. Jeong J. EEG dynamics in patients with Alzheimer's disease. Clin Neurophysiol. 2004;115:1490–505.
44. Gaubert S, Raimondo F, Houot M, Corsi MC, Naccache L, Diego Sitt J, et al. EEG evidence of compensatory mechanisms in preclinical Alzheimer's disease. Brain. 2019;142:2096–112.
45. Aggleton JP, Christiansen K. The subiculum: the heart of the extended hippocampal system. Prog Brain Res. 2015;219:65–82.
46. Matsumoto N, Kitanishi T, Mizuseki K. The subiculum: unique hippocampal hub and more. Neurosci Res. 2019;143:1–12.
47. Dalton MA, Maguire EA. The pre/parasubiculum: a hippocampal hub for scene-based cognition? Curr Opin Behav Sci. 2017;17:34–40.
48. Oakley H, Cole SL, Logan S, Maus E, Shao P, Craft J, et al. Intraneuronal beta-amyloid aggregates, neurodegeneration, and neuron loss in transgenic mice with five familial Alzheimer's disease mutations: potential factors in amyloid plaque formation. J Neurosci. 2006;26:10129–40.
49. Romoli M, Sen A, Parnetti L, Calabresi P, Costa C. Amyloid-beta: a potential link between epilepsy and cognitive decline. Nat Rev Neurol. 2021;17:469–85.
50. Yamazaki Y, Zhao N, Caulfield TR, Liu CC, Bu GJ. Apolipoprotein E and Alzheimer disease: pathobiology and targeting strategies. Nat Rev Neurol. 2019;15:501–18.
51. Chen D, Wang C, Chen X, Li J, Chen S, Li Y, et al. Brain-wide microglia replacement using a nonconditioning strategy ameliorates pathology in mouse models of neurological disorders. Sci Transl Med. 2025;17:eads6111.
52. Leng L, Zhuang K, Liu Z, Huang C, Gao Y, Chen G, et al. Menin deficiency leads to depressive-like behaviors in mice by modulating astrocyte-mediated neuroinflammation. Neuron. 2018;100:551–63.e7.
53. Zhuang K, Huang C, Leng L, Zheng H, Gao Y, Chen G, et al. Neuron-specific menin deletion leads to synaptic dysfunction and cognitive impairment by modulating p35 expression. Cell reports. 2018;24:701–12.
54. Alexovic M, Sabo J, Longuespee R. Microproteomic sample preparation. Proteomics. 2021;21:e2000318.
55. Gabitto MI, Travaglini KJ, Rachleff VM, Kaplan ES, Long B, Ariza J, et al. Integrated multimodal cell atlas of Alzheimer's disease. Nat Neurosci. 2024;27:2366–83.
56. Hou J, Chen Y, Cai Z, Heo GS, Yuede CM, Wang Z, et al. Antibody-mediated targeting of human microglial leukocyte Ig-like receptor B4 attenuates amyloid pathology in a mouse model. Sci Transl Med. 2024;16:eadj9052.

AUTHOR CONTRIBUTIONS

YC, **BJ**, **KZ and HW** contributed equally to this work; **JZ and LHZ** conceptualized the study; **YC** performed electrophysiological tests **YC**, **HP** and **TZ** maintained the mice, performed behavior tests and harvested tissue samples **BJ** and **HW** performed high resolution mass spectral test **HP** and **WX** carried out immunoblotting tests. **KZ**, **HW** and **B Z** gave advice on high resolution mass spectral data analysis. **KZ**, **KC** and **YW** performed immunostaining tests. **LZ** analyzed human snRNA-seq data. **JZ** and **LHZ** designed study and supervised the manuscript. **YC**, **BJ**, **KZ**, **HW** and **LZ** analyzed data and wrote manuscript. **HY**, **QY**, **JCZ**, **LZ**, **LHZ**, and **JZ** reviewed and edited the paper. All authors read and approved the final manuscript.

FUNDING

This study was supported by grants from the National Natural Science Foundation of China (U23A20430, 92149303, 81925010 and U1905207 to **JZ**, 22393931, 21991083 and 32088101 to **LHZ**, 22074140 and 22474136 to **BJ**, 82101242 to **KZ**, 32471045 and 82071198 to **LZ**), a grant from the National Key Research and Development Program of China (2021YFA1101402 to **JZ**), a grant from National Key R&D Program of China (2022YFC3401204 to **LHZ**), and supported by DICP (DICP I202316 to **BJ**).

COMPETING INTERESTS

The authors declare no competing interests.

ADDITIONAL INFORMATION

Supplementary information The online version contains supplementary material available at https://doi.org/10.1038/s41380-025-03217-4.

Correspondence and requests for materials should be addressed to Li Zhong, Li-Hua Zhang or Jie Zhang.